Vegetation browning patterns under compound soil and atmospheric dryness in northern permafrost ecosystems

nature communications

Article

https://doi.org/10.1038/s41467-026-75131-4

Vegetation browning patterns under compound soil and atmospheric dryness in northern permafrost ecosystems

Received: 9 June 2025

Accepted: 22 June 2026

Published online: 01 July 2026

Check for updates

Mousong Wu[1] ✉, Oliver Sonnentag[2] ✉, Mark J. Lara[3,4], Youhua Ran[5] ✉, Hans W. Chen[6], Wenxin Zhang[7,8], Philippe Ciais[9], Bo Elberling[10], Xin Li[11], Anping Chen[12], Songhan Wang[13], Yonghong Yi[14], Changhui Peng[15,16] & Deliang Chen[17,18]

Significant changes in vegetation greenness and browning have been observed across the northern permafrost zone, with important implications for ecosystem functioning and carbon uptake. While recent research has improved our understanding of the drivers of greening, the processes behind browning – especially the low-stature shrubs and herbaceous vegetation, which is more directly exposed to soil and atmospheric moisture deficits – remain less clear. To characterize browning patterns, we integrate multiple remote sensing datasets – including normalized difference vegetation index (NDVI), solar-induced chlorophyll fluorescence (SIF), and foliar chlorophyll concentration (FCC) – with gross primary productivity (GPP) simulations from CMIP6 Earth system models (ESM). We identify significant browning trends (−0.033 to −0.025 decade-1, from MODIS NDVI) from 2001 to 2018, affecting approximately 20 % (~600,000 km^2) of the study region. Browning is primarily modulated by compound soil and atmospheric dryness, reflected by declining soil moisture concurrent with increasing vapor pressure deficit. We further show that regional warming and changes in precipitation, together with permafrost-related constraints on infiltration and storage, modulate the spatial heterogeneity of compound dryness. CMIP6 projections suggest that compound dryness is likely to persist or intensify in permafrost ecosystems, implying continued risk of productivity loss, especially when combined with pulse disturbances such as wildfires.

In situ and remote sensing observations have revealed widespread vegetation 'greening' (i.e., increased vegetation productivity and/or biomass) alongside 'browning' (i.e., decreased vegetation productivity and/or biomass) across Arctic-boreal regions of Eurasia, North America, and the Tibetan Plateau under recent warming[1–3]. Much of this vast domain overlies permafrost (ground remaining frozen for at least two consecutive years)[4], where climate warming and increasingly frequent, intense pulse disturbances (e.g. wildfire) are accelerating permafrost thaw and degradation[5,6]. These changes have altered soil moisture and thermal regimes and can propagate through the soil-plant-atmosphere continuum, altering plant water stress, energy balance, and carbon uptake[7,8]. Because the permafrost region stores large carbon pools, uncertainty in how vegetation will respond to continued warming and disturbance directly translates into uncertainty in the net carbon balance of the permafrost zone and the strength of permafrost-carbon feedbacks[9].

A full list of affiliations appears at the end of the paper. ✉e-mail: mousongwu@nju.edu.cn; oliver.sonnentag@umontreal.ca; ranyh@lzb.ac.cn

Numerous studies have examined mechanisms linking warming to changes in vegetation productivity and biomass across permafrost landscapes. Permafrost warming and thaw, along with earlier snowmelt, can lengthen the growing season and enhance plant-available energy, moisture, and nutrients, promoting photosynthesis and growth[10]. However, warming can also intensify evaporative demand and, together with reductions in late-winter snow water equivalent, reduce water availability during the growing season, suppressing productivity[11,12]. In parallel, pulse disturbances – including wildfires[13], abrupt thaw and thermokarst formation[14], and extreme weather events[15] – can cause abrupt losses of vegetation biomass and persistent shifts in ecosystem functioning. Despite these advances, direct observational attribution of browning drivers remains limited and spatially uneven (e.g., concentrated in a small number of sites in Alaska and Siberia)[2,16,17]. Site-based evidence increasingly pointed to the joint role of soil moisture deficits and atmospheric dryness in triggering browning[18,19], yet how these interacting stressors scale to regional patterns across the permafrost zone remains poorly quantified.

Emerging remote sensing and in situ studies suggest that warming-induced soil drying and atmospheric moisture demand constrain plant growth, leading to stress, damage, or mortality that can manifest as widespread browning[20–22]. Much of the existing literature has focused on forests, emphasizing hydraulic strategies across species, canopy-understory buffering, and management and disturbance effects[21]. By contrast, the moisture-stress response of low-stature vegetation – shrubs and herbaceous plants – remains comparatively underexplored, despite their dominance across large fractions of the northern permafrost zone[23]. Over the past two decades, hydroclimatic variability and extremes have intensified in many high-latitude and high-elevation regions[2,19,24], potentially increasing exposure of low-stature plants to water limitation. Their shallow rooting systems and close coupling to near-surface microclimate make them especially vulnerable to compound soil and atmospheric dryness, where reduced root-zone soil moisture coincides with high vapor pressure deficit (VPD)[18,19]. Physiologically, soil moisture deficits can trigger stomatal regulation that reduces transpiration cooling and alters leaf-air humidity gradients, while high VPD increases atmospheric demand; together, these processes can amplify water stress and suppress carbon uptake[22,25]. Yet the extent to which compound dryness explains observed browning patterns across northern permafrost zone – and how its impact varies with regional climate background, permafrost and soil properties, surface water, vegetation characteristics, and disturbance history – remains unresolved.

Regional changes in vegetation productivity can be assessed using satellite indicators such as the normalized difference vegetation index (NDVI)[26], solar-induced chlorophyll fluorescence (SIF)[27], and foliar chlorophyll concentration (FCC)[28]. The expanding availability of long-term, high-quality satellite observations together with climate reanalysis products has provided an opportunity to diagnose broad-scale constraints on vegetation changes and to separate climatic from environmental and disturbance influences[29]. Here, we quantify spatial patterns of vegetation browning across permafrost regions in Eurasia, North America, and the Tibetan Plateau using multiple datasets for 2001 – 2018, focusing on low-stature shrubs and herbaceous vegetation. We test the hypothesis that browning is primarily modulated by compound soil and atmospheric dryness, and we diagnose the co-occurrence of soil moisture deficits and atmospheric dryness using the interannual correlation between mean growing-season root-zone soil moisture (RSM) and VPD, where more negative values indicate stronger concurrence of low RSM with high VPD. We further hypothesize that the strength of this relationship is modulated by regional controls – including climate, vegetation, soil/permafrost conditions, surface water, and wildfires – because these factors shape both plant-accessible water and atmospheric demand. We firstly identify browning using multiple satellite-derived datasets and benchmark patterns against Earth system model (ESM) simulations from the Coupled Model Intercomparison Project Phase 6 (CMIP6)[30]. We then evaluate relationships between compound dryness and browning across permafrost regions and assess the sensitivity of compound dryness to potential climatic, environmental, and disturbance controls. Finally, using CMIP6 projections under multiple shared socioeconomic pathways (SSPs)[30], we assess how future changes in compound dryness may influence vegetation productivity across permafrost ecosystems.

Results

Greening and browning across northern permafrost regions

The three major permafrost regions of the Northern Hemisphere span broad latitudinal and elevational gradients, encompass diverse climatic conditions, and are dominated by low-stature vegetation (Fig. S1; Suppl. Text S3). We delineated these regions by geography as: the Arctic-boreal region of Eurasia (EA), the Arctic-boreal region of North America (NA), and the Tibetan Plateau (TP) (Fig. 1a). Using MODIS NDVI (MCD43A4), we detected a significant ($P < 0.05$) increase in mean growing-season NDVI ($NDVI_{gs}$) across the northern permafrost zone, consistent with widespread greening. Over 2001–2018, $NDVI_{gs}$ increased by 0.021 ± 0.027 decade^{-1} (median ± 1 SD) in EA, 0.024 ± 0.022 decade^{-1} in NA, and 0.014 ± 0.021 decade^{-1} on the TP.

Despite the overall greening, browning remained a prominent feature within areas exhibiting significant $NDVI_{gs}$ trends. Among grid cells with significant $NDVI_{gs}$ trends, 21 % in EA, 8 % in NA, and 18 % on the TP showed significant declines in $NDVI_{gs}$ (Suppl. Text S4; Fig. 1a). These browning grid cells exhibited median (± 1 SD) $NDVI_{gs}$ trends of -0.033 ± 0.025 decade^{-1} in EA, -0.025 ± 0.012 decade^{-1} in NA, and -0.033 ± 0.014 decade^{-1} on the TP. In terms of area, browning spanned 4.30×10^5 km^2 in EA, 1.81×10^5 km^2 in NA, and 1.34×10^4 km^2 on the TP. Spatially, browning was concentrated in cold-humid zones of EA and NA, and in warm, semi-arid zones of the TP (Figure S1).

These patterns were supported by multiple remote sensing products (Table S1), which yielded broadly consistent estimates of browning among grid cells with significant trends ($P < 0.05$) in vegetation indices: 25 ± 8% (EA), 23 ± 9% (NA), and 18 ± 11% (TP) of the permafrost zone (Fig. 1b). In contrast, CMIP6 Earth system models (14 ESMs) showed substantial inter-model spread in their ability to reproduce the observed spatial distribution of greening and browning (Fig. S4; Table S3). While the multi-model ensemble produced browning percentages comparable to satellite products, simulated mean growing-season GPP (GPP_{gs}) indicated smaller – and in some regions statistically insignificant – browning percentages: 19 ± 15% in EA, 17 ± 23% in NA, and 1 ± 13% on the TP for 2000–2014 (Fig. 1b; Table S2; Suppl. Text S4). Several models simulated little to no browning percentages over NA and the TP, highlighting limitations and structural differences among ESMs in representing permafrost vegetation responses.

Compound soil and atmospheric dryness modulates browning

The co-variability between root-zone soil moisture and vapor pressure deficit provides a useful diagnostic of land-atmosphere hydroclimatic interactions[21,22,31]. Here we quantified this co-variability as the Pearson correlation $r(RSM_{gs}, VPD_{gs})$ as mean growing-season conditions. Negative values indicate that years with higher atmospheric moisture demand (higher VPD_{gs}) tend to coincide with lower soil moisture (lower RSM_{gs}), consistent with compound soil and atmospheric dryness. Across browning areas, $r(RSM_{gs}, VPD_{gs})$ was negative in 87–95% of grid cells, and 41 % of grid cells showed significantly negative co-variability ($P < 0.05$; $r < -0.5$) (Fig. 2a). Consistent with this diagnostic, 98%, 98%, and 70% of browning areas in EA, NA, and the TP, respectively, experienced both decreasing RSM_{gs} and increasing VPD_{gs} (Fig. 2b; Fig. S7).

We further found a significant relationship ($r = -0.35$, $P < 0.001$) between $r(NDVI_{gs}, VPD_{gs})$ and $r(NDVI_{gs}, RSM_{gs})$ (Fig. 2c; Fig. S8),

https://doi.org/10.1038/s41467-026-75131-4

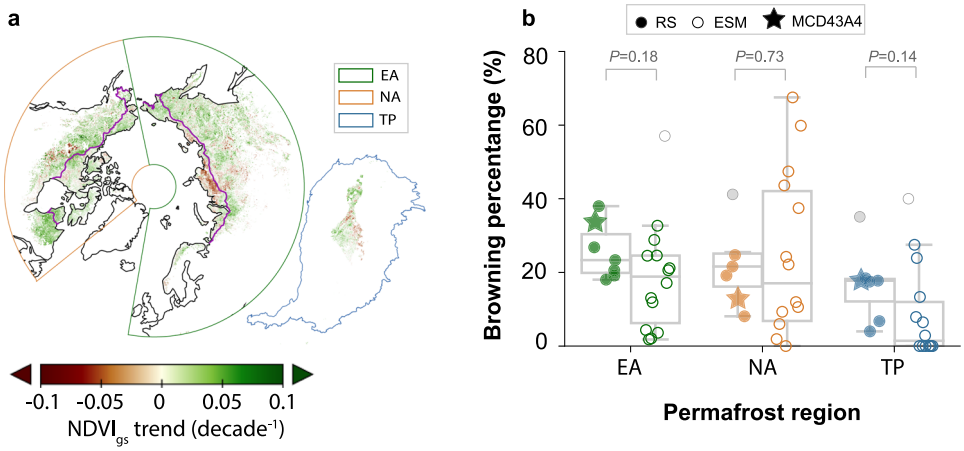

Fig. 1 | Greening and browning in three northern permafrost regions. a Spatial distribution of significant ($P < 0.05$) mean growing season NDVI ($NDVI_{gs}$) trends from MODIS (MCD43A4) in permafrost regions of Eurasia (EA), North America (NA), and the Tibetan Plateau (TP, enlarged for clarity) in 2001–2018. The purple line outlines the circumpolar Arctic vegetation map (CAVM) extent[60]. **b** Boxplots for significant ($P < 0.05$) browning percentages relative to all grid cells with significant trends estimated through satellite remote sensing (RS) data products (dots, $n = 7$) including MODIS (MCD43A4) (star) and by historical CMIP6 Earth system model (ESM) ensemble simulations (circles, $n = 14$). Grey dots and circles denote outliers. Boxes denote the 1st and 3rd quantiles, whiskers denote the minimum and maximum values, and horizontal lines denote the median values. Source data are provided as a Source Data file. Basemap from GeoPandas (http://geopandas.org)[83]. Boundary of the Tibetan Plateau from National Earth System Science Data Center (http://www.geodata.cn).

indicating that years in which vegetation greenness is more sensitive to atmospheric dryness also tend to be those in which it is more sensitive to soil moisture deficits. To reveal how compound dryness maps onto productivity anomalies, we binned standardized anomalies of $NDVI_{gs}$ by corresponding anomalies of VPD_{gs} and RSM_{gs} (Fig. 2d–f; Fig. S6). In EA, $NDVI_{gs}$ tended to be higher under higher RSM_{gs} while its relationship with VPD_{gs} was weaker and spatially heterogeneous (Fig. 2d). In NA, browning areas showed a stronger dependence of $NDVI_{gs}$ on RSM_{gs}, with consistently lower $NDVI_{gs}$ under lower soil moisture regardless of VPD_{gs} (Fig. 2e). On the TP, lower $NDVI_{gs}$ decreased under the combined influence of lower RSM_{gs} and higher VPD_{gs}, consistent with concurrent soil and atmospheric moisture constraints (Fig. 2f). Although previous studies have suggested that the TP has generally become wetter in recent decades[32], we detected increasing VPD_{gs} in ~70 % of browning areas and only marginally changes in RSM_{gs} (Fig. S7), underscoring the prominent role of atmospheric dryness in the TP browning (Fig. S8; Suppl. Text S5).

Next, we examined how $r(VPD_{gs}, RSM_{gs})$ is linked to browning extent across regions. The TP exhibited the most negative $r(VPD_{gs}, RSM_{gs})$ values, indicating the strongest anti-phase co-variability between RSM_{gs} and VPD_{gs} (Fig. 3a). The relationship between $r(VPD_{gs}, RSM_{gs})$ and browning extent was region-dependent: browning extent increased with more negative $r(VPD_{gs}, RSM_{gs})$ in NA and on the TP ($P < 0.001$), whereas the relationship was reversed in EA ($P < 0.001$), likely reflecting heterogeneous temperature controls and hydrothermal regimes across EA browning areas (Fig. S9). In CMIP6 simulations, GPP_{gs} showed broadly positive relationships with $r(VPD_{gs}, RSM_{gs})$ across the three regions, but with substantial inter-model spread (Fig. 3b; Fig. S11), highlighting persistent uncertainty in how current ESMs represent vegetation responses to compound soil and atmospheric dryness at regional scales. CMIP6 projections further indicate a decline in $r(VPD_{gs}, RSM_{gs})$ of approximately −0.01 per decade ($P < 0.001$) under future scenarios (Fig. S12), suggesting that the adverse impacts of compound dryness on browning are likely to intensify.

We then used standardized anomalies to disentangle the contributions of VPD_{gs} and RSM_{gs} to $NDVI_{gs}$ by decoupling their covariation[25] (Fig. 3c, d, *Methods: Statistical analysis*). The contribution of VPD_{gs} to $NDVI_{gs}$, while controlling for RSM_{gs} ($C_{VPD|RSM}$) increased from EA and NA to the TP, with a significant difference between the TP and NA ($P < 0.05$), indicating a stronger atmospheric-dryness constraint at high elevations than at high latitudes. In contrast, the contribution of RSM_{gs} while controlling for VPD_{gs} ($C_{RSM|VPD}$) was not significantly different from zero in EA ($P > 0.05$), but was significantly positive in NA and on the TP ($P < 0.05$), indicating a transition from weak/indistinguishable soil-moisture control in EA to stronger soil-moisture limitation in NA and the TP.

Drivers of compound soil and atmospheric dryness

We evaluated 14 candidate controls on compound soil and atmospheric dryness across browning areas, and used $r(VPD_{gs}, RSM_{gs})$ as a diagnostic indicator of the co-occurrence of low soil moisture with high atmospheric moisture demand. Candidate variables were grouped into five categories – climate, vegetation, soil/permafrost, surface water (e.g., lakes and ponds), and wildfires – and their relative importance was assessed using an explainable machine-learning framework[33] (*Methods: Identifying the controls on compound dryness*). Across browning areas, climate variables were the dominant predictors, while soil/permafrost variables ranked second overall (Fig. S13; Supplementary Text 6). In greening areas, soil/permafrost variables showed higher relative importance than in browning areas (Fig. S13), highlighting that the controls on soil-atmosphere co-variability differ between greening and browning regimes. Among individual predictors, permafrost continuity, active-layer thickness, or permafrost hydrothermal conditions emerged as influential factors in the TP, EA, and NA browning areas, respectively. Vegetation-related variables consistently contributed additional explanatory power, whereas surface water and wildfire metrics had comparatively smaller importance, indicating that regional climate background and soil/permafrost state jointly shape the co-occurrence of soil moisture deficits and atmospheric dryness in browning regions.

To interpret how specific variables modulate $r(VPD_{gs}, RSM_{gs})$ in browning areas, we examined accumulated local effects (ALEs) plots[34]. In EA and NA, stronger warming was associated with more negative $r(VPD_{gs}, RSM_{gs})$ (Fig. 4a, b), implying an enhanced tendency for low soil moisture to co-occur with high atmospheric moisture demand. On the TP, increasing growing-season precipitation was associated with less negative $r(VPD_{gs}, RSM_{gs})$ (Fig. 4c), consistent with precipitation alleviating the co-occurrence of soil and atmospheric dryness. Across regions, more negative $r(VPD_{gs}, RSM_{gs})$ was

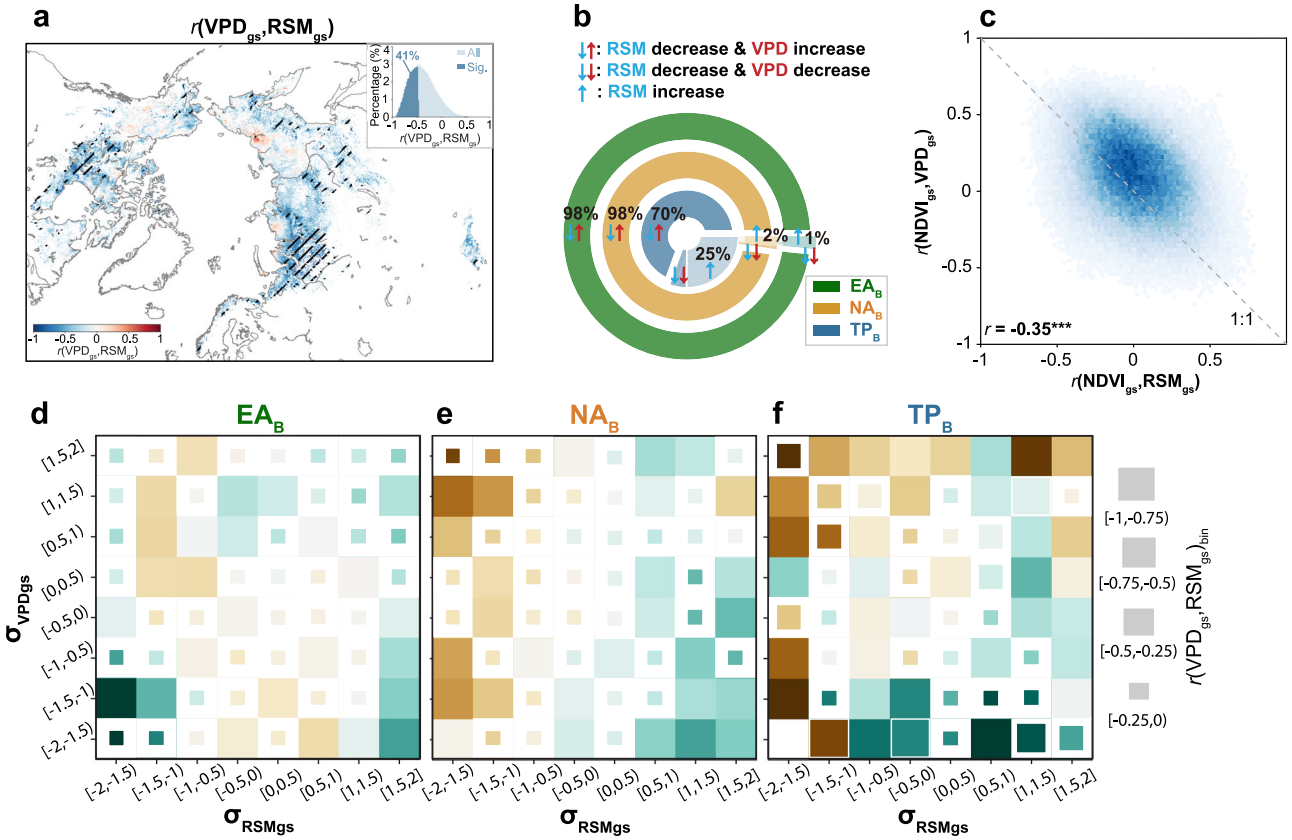

Fig. 2 | Compound soil and atmospheric dryness and its relationship with vegetation browning across three northern permafrost regions. a Interannual co-variability between mean growing-season root-zone soil moisture (RSMgs) and vapor pressure deficit (VPDgs) over browning areas, quantified as the Pearson correlation r(VPDgs, RSMgs). More negative values indicate stronger anti-phase co-variability, i.e., lower soil moisture co-occurring with higher atmospheric moisture demand. Hatching denotes grid cells with significant correlations ($P < 0.05$). The inset shows the percentage of grid cells with significant correlations relative to all browning grid cells. **b** Percentages of browning areas exhibiting different combinations of VPD_{gs} and RSM_{gs} trends. **c** Relationships between $r(NDVI_{gs}, VPD_{gs})$ and $r(NDVI_{gs}, RSM_{gs})$ across browning zones. Color indicates point density (darker denotes higher density). **d**–**f** Binned means of standardized $NDVI_{gs}$ anomalies (σ_{NDVIgs}) as a function of standardized anomalies of RSM_{gs} (σ_{RSMgs}) and VPD_{gs} (σ_{VPDgs}) for browning areas in Eurasia (EA_B), North America (NA_B) and the Tibetan Plateau (TP_B). Square size indicates the magnitude of negative $r(VPD_{gs}, RSM_{gs})$, representing the strength of compound dryness co-occurrence. Source data are provided as a Source Data file. Basemap from GeoPandas (http://geopandas.org)[83].

generally linked to reduced permafrost continuity, limited active-layer deepening (below a threshold), and more humid background conditions, whereas less negative $r(VPD_{gs}, RSM_{gs})$ tended to occur under shallower mean active layers (Fig. S16). Together, these patterns suggest that active-layer deepening can partially alleviate near-surface water limitations by increasing plant-accessible soil water in some browning areas. Finally, a longer growing season was associated with more negative $r(VPD_{gs}, RSM_{gs})$ in EA and NA (above a threshold), but less negative $r(VPD_{gs}, RSM_{gs})$ on the TP. This contrast may reflect differing hydroclimatic constraints: the TP exhibits a narrower RSM_{gs} range than EA and NA (Fig. S8), such that longer seasons can amplify atmospheric demand without a commensurate increase in soil water supply, weakening the interannual co-variability between soil moisture and VPD.

Discussion

We investigated how compound soil and atmospheric dryness – characterized by co-occurring root-zone soil moisture deficits (low RSM_{gs}) and elevated atmospheric moisture demand (high VPD_{gs}) – controls vegetation browning across the northern permafrost zone. Using multiple remote-sensing products and simulations from CIMP6 Earth system models, we revealed that browning during 2001 – 2018 is widespread yet spatially heterogeneous, with browning areas accounting for ~20 % of the permafrost zone. Across browning areas, the interannual co-variability between soil moisture and atmospheric demand, quantified as $r(VPD_{gs}, RSM_{gs})$, provided a useful diagnostic of when soil moisture deficits tend to coincide with elevated VPD, consistent with compound dryness. Our results indicate that this diagnostic – and the underlying hydroclimatic regime it reflected – vary systematically across Eurasia, North America, and the Tibetan Plateau, with important implications for the regional vulnerability of low-stature vegetation.

To identify why compound dryness differs across regions, we assessed the relative importance of climatic, soil/permafrost, and vegetation controls and explored their nonlinear effects. Climatic factors emerged as the dominant controls, with soil/permafrost and vegetation factors providing additional, region-specific modulation. In Eurasia, permafrost continuity was among the most influential soil-related predictors in browning areas, consistent with the role of continuous permafrost in limiting subsurface drainage and shaping near-surface water availability. Areas with high permafrost continuity (areal continuity > 90%) can act as hydrological barriers that constrain vertical and lateral water redistribution, potentially strengthening the co-occurrence of shallow soil moisture deficits with atmospheric dryness under warming[35]. In contrast, on the Tibetan Plateau, growing-season phenological constraints (e.g., length of growing season) exerted a stronger influence than several soil-related predictors, consistent with the plateau's distinct permafrost characteristics, including generally deeper active layers and lower ground-ice content relative to Arctic lowlands[16,36] (Fig. S16; Suppl.

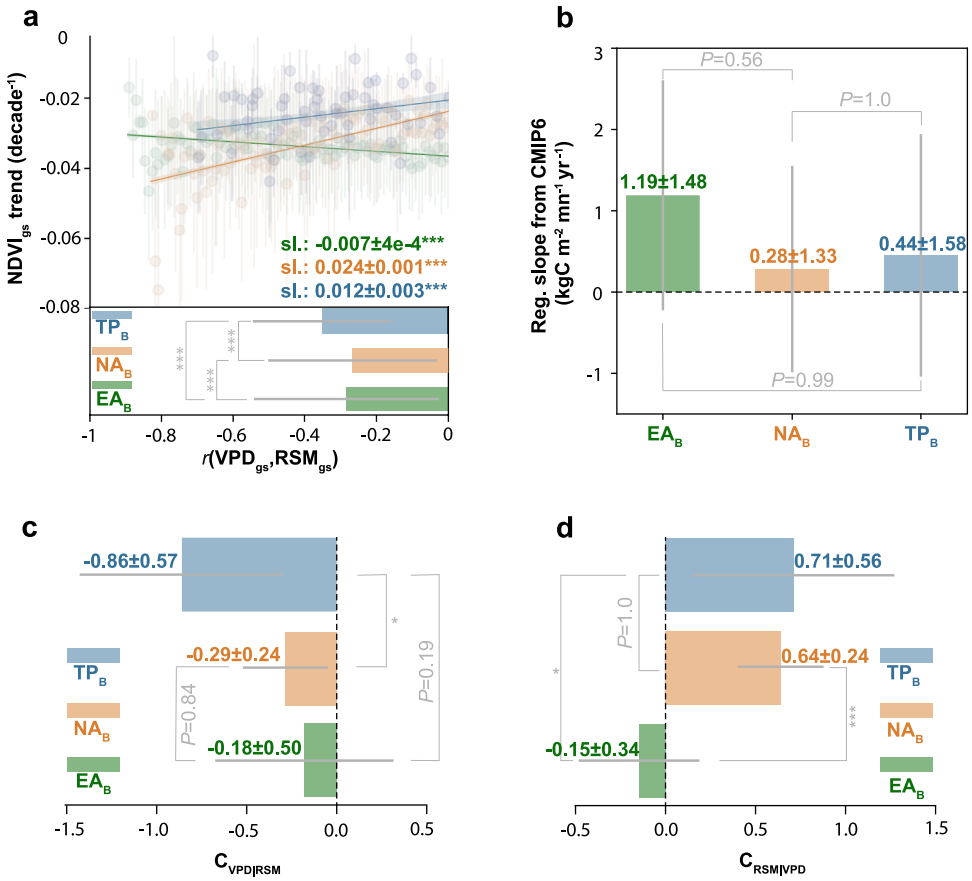

Fig. 3 | Compound soil and atmospheric dryness and its contribution to vegetation browning across three northern permafrost regions. a Relationships between browning trends and interannual soil-atmosphere co-variability quantified as the Pearson correlation r(VPD$_{gs}$, RSM$_{gs}$) for grid cells with significant ($P < 0.05$) browning trends in Eurasia (EA$_B$), North America (NA$_B$), and the Tibetan Plateau (TP$_B$). Points show the mean (dot) and standard deviation (error bar) across 100 equal-count bins. Regression lines are fitted using all grid cells within each region; shading indicates 95% confidence intervals. The slope (sl.) is reported with significance indicated by asterisks ($P < 0.001$). The lower bar plot summarizes r(VPD$_{gs}$, RSM$_{gs}$) for each region, with bar for mean and error bar for the standard deviation for all grid cells. **b** Regression slopes relating simulated mean growing-season gross primary productivity (GPP$_{gs}$) to r(VPD$_{gs}$, RSM$_{gs}$) from 14 CMIP6 Earth system models (historical simulations); bar denotes the mean and error bar denotes the inter-model standard deviation ($n = 14$). **c** Contributions of standardized VPD$_{gs}$ anomalies to browning while controlling for standardized RSM$_{gs}$ anomalies (C$_{VPD|RSM}$) across permafrost regions. **d** Contributions of standardized RSM$_{gs}$ anomalies to browning while controlling for standardized VPD$_{gs}$ anomalies (C$_{RSM|VPD}$) across permafrost regions. Boxes denote bin means, and error bars denote standard deviations across eight bins ($n = 8$). Differences are labeled with P-values, *$P < 0.05$, **$P < 0.01$, and ***$P < 0.001$ or the P-value (insignificant). Source data are provided as a Source Data file.

Text S7). These regional contrasts in permafrost characteristics highlight that compound dryness is not governed by a single mechanism, but instead emerges from the interaction between atmospheric demand, plant phenology, and permafrost-regulated soil water supply[37,38] (Fig. 5).

Although pulse disturbances such as wildfires can strongly affect ecosystem structure and function, our analysis suggests that, over 2001–2018, wildfire-related predictors contributed less to explaining spatial variation in compound dryness diagnostics than climate, soil/permafrost, and vegetation factors. Only ~3.3–4.5% of 0.05° × 0.05° grid cells within browning areas experienced wildfire events during the study period. These burned areas exhibited slightly reduced vegetation productivity, but the long-term effect was no significant (Fig. S17), consistent with the idea that browning patterns at regional scales are more strongly shaped by hydroclimatic constraints than by the limited fraction of burned grid cells over this period[24]. Nevertheless, continued warming is expected to increase wildfire frequency and extent, and interactions between fire, permafrost thaw, and post-fire recovery may intensify in coming decades[39–41]. Such feedbacks could further destabilize permafrost, alter hydrological regimes, and increase the likelihood of transitions from net carbon sinks to net carbon sources[42].

Surface water bodies were present in 6.5–61.2% of browning grid cells, yet we did not detect a clear relationship with long-term vegetation productivity trends (Fig. S17). This apparent weak signal may reflect competing mechanisms. Waterlogged or anoxic conditions can constrain plant growth in wet landscapes[37,43–45], whereas in dry areas or during drought episodes, nearby lakes and ponds can enhance local moisture availability and create favorable microhabitats that support vegetation growth[29,43,46,47]. In permafrost regions, thaw-driven changes in hydrological connectivity can further shift the balance between these mechanisms by reorganizing drainage pathways and redistributing water across the landscape[18,29,43,48]. Together, these processes likely contribute to divergent productivity trajectories across permafrost ecosystems and underscore the need to represent hydrothermal feedbacks more explicitly in both data-driven analyses and process-based models.

We acknowledge several sources of uncertainty. Differences between NDVI and GPP in representing vegetation productivity and long-term trends, inter-sensor consistency, and potential sensor degradation[49]. However, the use of multiple satellite products – including SIF as a proxy for photosynthesis – provides convergent evidence for the broad patterns reported here. Moreover, the spatial resolution of NDVI data limits our ability to assess the local ecological

https://doi.org/10.1038/s41467-026-75131-4

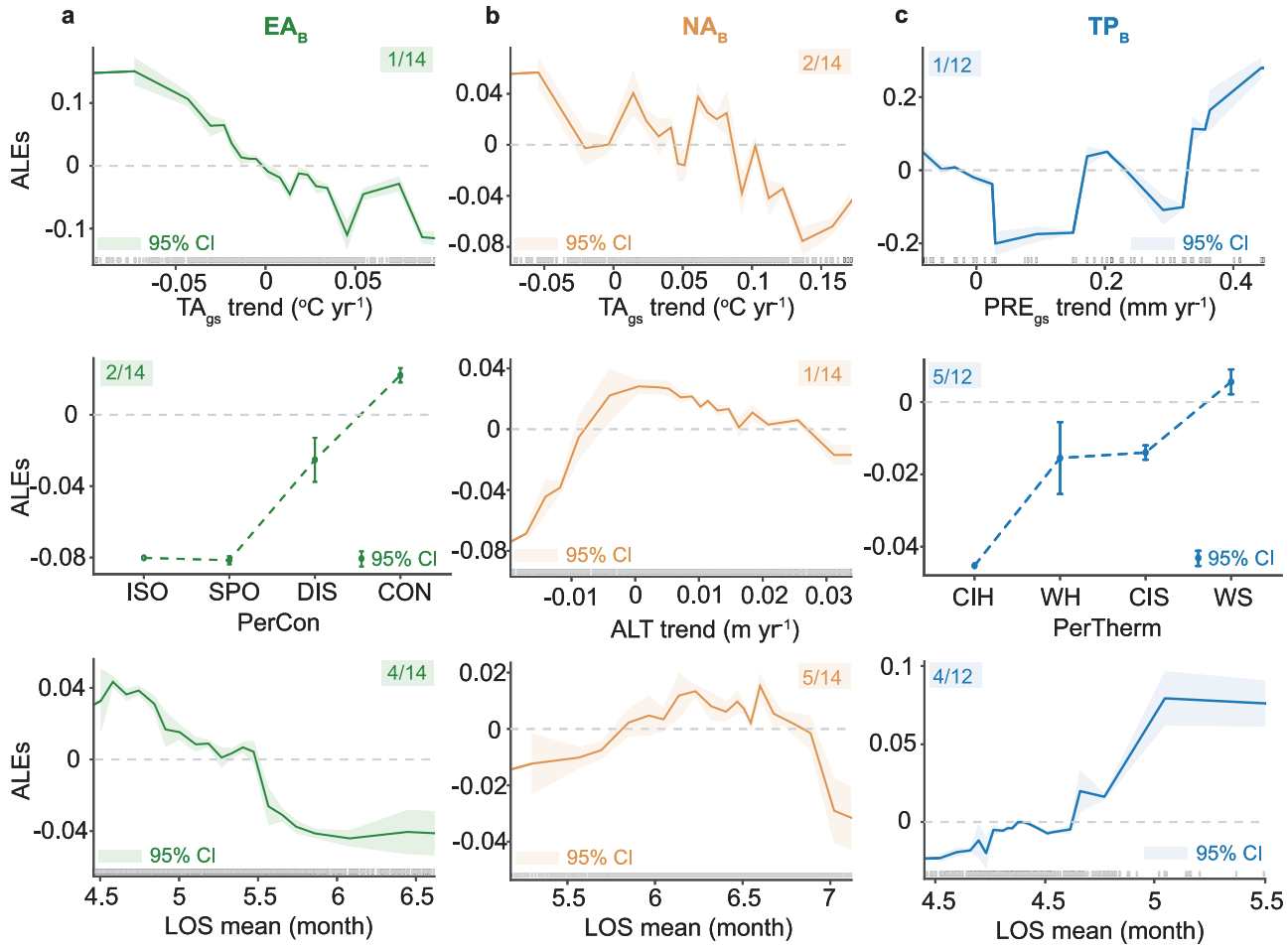

Fig. 4 | Accumulated local effects (ALEs) of key controls on co-occurrence of compound soil and atmospheric dryness, diagnosed by $r(VPD_{gs}, RSM_{gs})$, in browning areas across three northern permafrost regions. Shown are ALE curves for the three highest-ranked predictors (from the climate, soil/permafrost, and vegetation groups) explaining the interannual co-variability between mean growing-season root-zone soil moisture and vapor pressure deficit, quantified as $r(VPD_{gs}, RSM_{gs})$, in browning areas of (**a**), Eurasia (EA_B), (**b**), North America (NA_B), and (**c**), on the Tibetan Plateau (TP_B). Shading denotes the 95 % confidence interval (CI) of ALE estimates. Rug plots show the distribution of predictor values. The grey dashed horizontal line indicates zero effect, and the x-axis spans the 2.5th – 97.5th percentiles of each predictor. Numbers in each panel indicates predictor rank among all candidates. TA_{gs} mean growing season air temperature, PerCon Permafrost continuity classification (ISO isolated, SPO sporadic, DIS discontinuous, CON continuous), LOS length of growing season, ALT active-layer thickness, PRE_{gs} is mean growing-season mean precipitation; and PerTherm is hydrothermal conditions of permafrost (CIH cool-humid, WH warm-humid, CIS cool-semi-arid, WS warm-semi-arid). "trend" denotes 2001–2018 temporal trend, and "mean" denotes 2001–2018 average. Source data are provided as a Source Data file.

drivers of browning, such as vegetation mortality or changes in species composition[1]. We highlight the need for more consistent, long-term datasets to better constrain these dynamics in future studies. A key additional uncertainty arises from model representation: many ESMs struggle to reproduce observed spatial patterns of productivity change, particularly in regions experiencing rapid permafrost degradation such as the North American Arctic-boreal zone and the Tibetan Plateau[50]. These discrepancies raise concerns about the robustness of future projections and point to missing or misrepresented processes, including active-layer thickening, thermokarst development and expansion, and thaw-driven changes in hydrological connectivity and soil-vegetation feedbacks[51]. Improving model skill will require explicit representation of permafrost-specific hydrothermal dynamics and their coupling to plant water stress and carbon uptake[52–57].

Together, our results reveal how compound soil and atmospheric dryness modulate vegetation browning across diverse permafrost landscapes. As warming and permafrost degradation accelerate, the sensitivity of low-stature vegetation to compound dryness may increase, with potential consequences for regional carbon balance and permafrost-carbon feedbacks.

Methods

Study region

We defined the northern permafrost zone as the permafrost regions of Eurasia (EA), North America (NA) and the Tibetan Plateau (TP), following the permafrost extent dataset of Obu et al.[58]. We focused on low-stature vegetation, and therefore intersected the permafrost extent with plant functional types (PFTs) derived from the MODIS land-cover product MCD12Q1 (v061). Using the International Geosphere-Biosphere Programme (IGBP) classification[59], we retained grid cells classified as grasslands, shrublands, and savannas (tree cover < 30%) to mask the study area. These PFTs cover the dominant low-stature vegetation types across the circumpolar Arctic vegetation domain (CAVM)[60] and the low-tree-cover savanna regions that occur within the permafrost zone[59]. We additionally included the Tibetan Plateau by selecting these three PFTs where underlain by permafrost (Suppl. Text S3).

Analyses were conducted at 0.05° × 0.05° spatial resolution and focused on grid cells exhibiting significant ($P < 0.05$) vegetation productivity trends, as these locations capture the most pronounced changes over the past two decades. We excluded wetlands identified at 0.05° × 0.05° resolution because mixed water/vegetation grid cells and

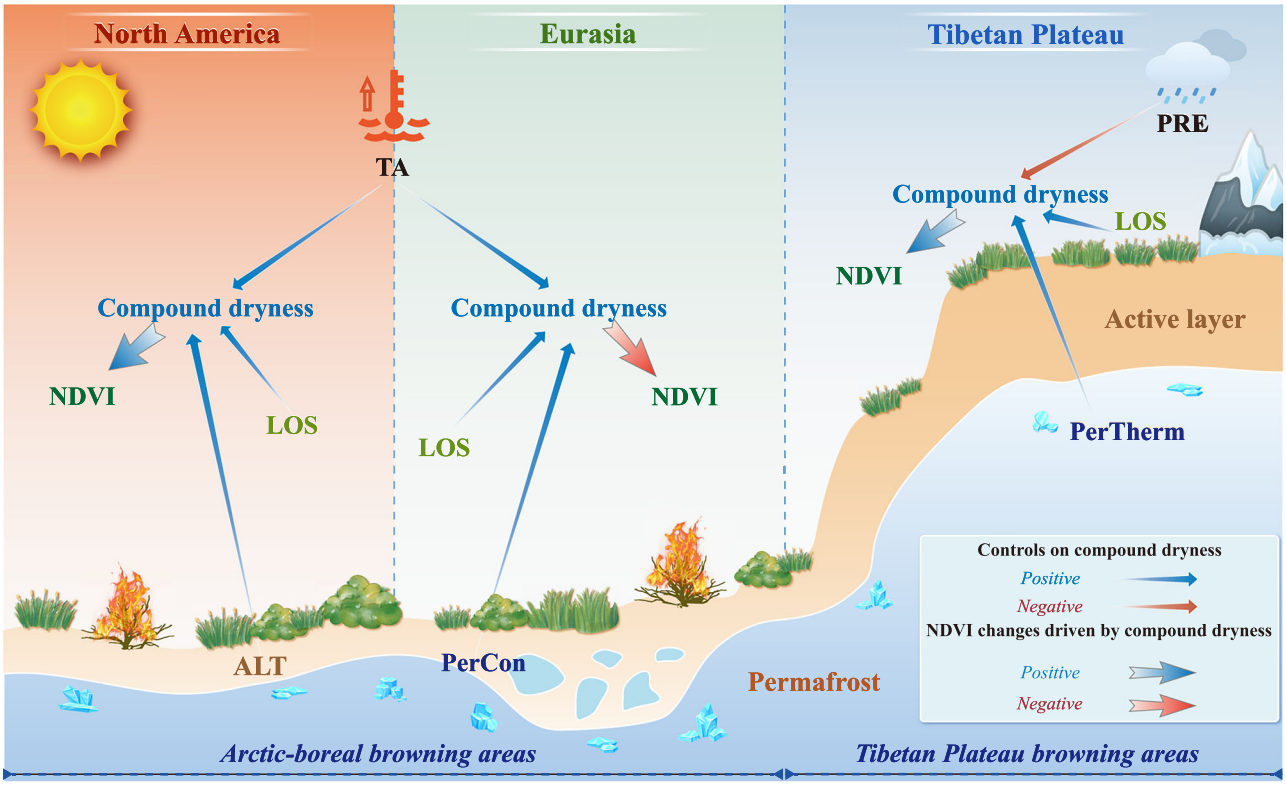

Fig. 5 | Drivers of compound soil and atmospheric dryness and its link to vegetation browning across permafrost regions in Eurasia (EA_B), North America (NA_B), and the Tibetan Plateau (TP_B). Acronyms are defined as: NDVI normalized difference vegetation index), TA air temperature, VPD vapor pressure deficit, PRE precipitation, RSM root-zone soil moisture, ALT active-layer thickness, PerCon permafrost continuity, PerTherm permafrost hydrothermal conditions, LOS length of growing season. Soil and atmospheric dryness diagnostic is quantified as the Pearson correlation $r(VPD_{gs}, RSM_{gs})$. For controls on compound dryness, a positive arrow to compound dryness indicates drier soil and atmosphere will be induced by the increased value in the variables, and vice versa for the negative arrow. Figure and its elements are created with Adobe Illustrator 2026.

water-related reflectance effects can bias optical retrievals of vegetation dynamics[29,46,61].

Data

We used the MODIS normalized difference vegetation index (NDVI) data over 30°–90° N for 2001–2018 derived from MCD43A4 (v061)[26]. The dataset was quality-filtered (removing cloud-affected observations) and screened for low NDVI values (< 0.1), then aggregated to monthly time steps and resampled to 0.05° × 0.05°. To assess robustness across sensors and retrieval algorithms, we also used additional NDVI products (MOD13A2 v061, MYD13A2 v061[62], PKU_GIMMS[63], SPOT-VGT/PROBA-V[64,65]), a reconstructed long-term solar-induced florescence product (LT_SIFc)[27], and foliar chlorophyll concentration (FCC)[66] to identify greening and browning patterns across platforms and products (Supplementary Data 1).

For independent site-scale evaluation, we used Landsat NDVI time series for 59 permafrost-underlain sites compiled in previous studies[42,67,68], extracting NDVI within a 1000 m buffer for 2001–2018. We used NDVI rather than carbon fluxes because long-term (e.g.,> 15 years) flux records from eddy covariance or chamber measurements remain sparse across permafrost regions, limiting robust trend assessment. The Landsat-based evaluation therefore, provides an independent estimate of vegetation productivity dynamics at local scales.

To characterize atmospheric and soil moisture conditions, we used vapor pressure deficit (VPD) and root-zone soil moisture (RSM). RSM was obtained from GLDAS_v021[69]. VPD was derived from ERA5[70] using 2-m air temperature (TA) and dewpoint temperature (TD) following ref. 71:

$$VPD = 610.78 \times e^{(17.27 \times TA/(TA+237.19))} - 610.78 \times e^{(17.27 \times TD/(TD+237.19))} \quad (1)$$

We further analyzed outputs from 14 Earth system models from the Coupled Model Intercomparison Project Phase 6 (CMIP6) simulation ensemble (Table S1), including historic simulations for 2000–2014 and future projections for 2020–2100 under the SSP1-2.6, SSP2-4.5, and SSP5-8.5. These models provide gross primary productivity (GPP), RSM, and variables required to compute VPD (calculated from model air temperature and relative humidity following ref. 72).

To investigate controls on browning and compound dryness diagnostics, we compiled 14 ancillary gridded datasets (Suppl. Data 1). These include growing-season climate variables from ERA5 (2 m air temperature TA, precipitation PRE, and surface net shortwave radiation Rn)[70] aggregated to 0.05° × 0.05° for 2001–2018. Permafrost extent and permafrost continuity (PerCon) were defined using mean annual ground temperatures (MAGT) at the zero annual amplitude depth[36,58]. Permafrost hydrothermal class (PerTherm) was defined using MAGT and a climate aridity index[36]. Active-layer thickness (ALT) and its temporal trend were obtained from ESA CCI[73] to characterize permafrost status[74]. Soil texture was taken from the Harmonized World Soil Database (HWSD v2.0)[75]. Length of growing season (LOS) and its trend were estimated from MODIS NDVI using a double-logistic approach implemented in TIMESAT v3.3[76,77]. Root depth was derived from HWSD v2.0, and land cover (LC) was taken from MCD12Q1 (v061). We additionally used accumulated fire burnt counts (BCount) from

Fire_cci v5.1[78] for 2001 – 2018 and annual mean water-body fraction (WFrac) from MOD44W v6.0[79] for 2001–2015. All ancillary datasets were aggregated to 0.05° × 0.05° to ensure spatial consistency across analyses.

Compound soil and atmospheric dryness

For each grid cell, we quantified the interannual co-variability between growing-season root-zone soil moisture and atmospheric moisture demand as the Pearson correlation coefficient $r(VPD_{gs}, RSM_{gs})$, computed from time series of mean growing-season root-zone soil moisture (RSM_{gs}; GLDAS_v2) and mean growing-season vapor pressure deficit (VPD_{gs}; derived from ERA5 air temperature and dew point temperature). The correlation ranges from −1 to +1. Negative $r(VPD_{gs}, RSM_{gs})$ indicates that years with higher atmospheric dryness (higher VPD_{gs}) tend to coincide with lower soil moisture (lower RSM_{gs}), consistent with the co-occurrence of soil moisture deficits and elevated atmospheric demand (i.e., compound soil and atmospheric dryness)[22]. Positive $r(VPD_{gs}, RSM_{gs})$ indicates that VPD_{gs} and RSM_{gs} vary in the same direction across years (e.g., both increase), which can arise under sustained wetting, lateral hydrological inputs, or thaw-driven changes in hydrological connectivity, among other processes. Because the majority (> 90%) of browning grid cells exhibited negative $r(VPD_{gs}, RSM_{gs})$ across all three permafrost regions, our regional analyses focus on grid cells exhibited negative $r(VPD_{gs}, RSM_{gs})$ unless stated otherwise. We computed the same diagnostic using CMIP6 outputs for the historical period 2000 – 2014 and for the future period 2020–2100. For future projections, we estimated $r(VPD_{gs}, RSM_{gs})$ using a 20-year moving window for each region under three scenarios (SSP1-2.6, SSP2-4.5, and SSP5-8.5).

Identifying controls on compound dryness

We employed extreme gradient boosting (XGBoost) model[33] to model spatial variation in $r(VPD_{gs}, RSM_{gs})$ as a function of 14 climatic and environmental predictors across the three northern permafrost regions (Suppl. Data 1). Model performance was evaluated using 10-fold cross validation repeated three times, and assessed using mean absolute error (MAE) and the coefficient of determination (R^2). To interpret predictor effects, we used accumulated local effects (ALEs) plots[80], which quantify the average marginal influence of each predictor on model predictions and are robust to correlated features. We applied the XGBoost plus ALEs framework separately for greening and browning regions to compare differences in their dominant controls. ALE curves were reported as the mean effect with 95 % confidence intervals (CI). We further verified the impacts of excluding forests from permafrost regions on the robustness of our conclusions (Suppl. Text S8).

Statistical analysis

Trends in growing-season variables were assessed using the non-parametric Mann-Kendall test with Sen's slope estimator[81]. Unless stated otherwise, trends were computed from annual growing-season means, and statistical significance was evaluated at $P < 0.05$. Variable anomalies were calculated as departure from the multi-year mean for each grid cell.

To disentangle the individual influences of atmospheric moisture demand and soil water supply on vegetation productivity, we applied a decoupling approach based on binned standardized anomalies[25]. Specifically, we examined relationships between mean growing-season NDVI ($NDVI_{gs}$) and VPD_{gs} or RSM_{gs} using the binned anomaly framework described in Suppl. Text S1. We also derived the maximum extent of browning to characterize the prevalence of browning within permafrost regions (Supplementary Text S2).

To relate the browning to compound dryness diagnostics, we used ordinary least squares regression to estimate the slope between browning metrics (e.g., $NDVI_{gs}$ trends) and the interannual soil-atmosphere co-variability $r(VPD_{gs}, RSM_{gs})$, reporting slope estimates with 95 % confidence intervals and corresponding P values. All statistical significance values reported in this paper were assessed using two-sided student's t-test. Differences among datasets were assessed using the non-parametric Mann-Whitney U test[82].

Reporting summary

Further information on research design is available in the Nature Portfolio Reporting Summary linked to this article.

Data availability

All data sources used in this study are listed in Supplementary Data 1 with links. The information of permafrost sites is provided in Supplementary Data 2. MODIS MCD43A4 NDVI data are derived from https://lpdaac.usgs.gov/products/mcd43a4v061/. MOD13A2 NDVI data are derived from http://lpdaac.usgs.gov/products/mod13a2v061/. MYD13A2 NDVI data are derived from https://lpdaac.usgs.gov/products/myd13a2v061/. The SPOT-VGT/PROBA-V NDVI data are available from https://dataspace.copernicus.eu/spot-vegetation; https://earth.esa.int/eogateway/missions/proba-v. Landsat NDVI data are derived from https://www.usgs.gov/landsat-missions/data. Processed gridded datasets used to generate figures and tables are available on the National Cryosphere Desert Data Center (https://doi.org/10.12072/ncdc.permafrost.db7313.2026) and National Tibetan Plateau Data Center (https://doi.org/10.11888/Cryos.tpdc.303386). Source data are provided with this paper.

Code availability

The analysis scripts (Python 3.9) used to process the input data, conduct analysis, and produce figures are available on GitHub (https://github.com/mswu027/Permafrost-ecosystem-browning-analysis) and archived at Zenodo (https://doi.org/10.5281/zenodo.20341418).

References

1. Treharne, R., Bjerke, J. W., Tømmervik, H. & Phoenix, G. K. Development of new metrics to assess and quantify climatic drivers of extreme event driven Arctic browning. *Remote Sens. Environ.* **243**, 111749 (2020).
2. Treharne, R., Bjerke, J. W., Tømmervik, H., Stendardi, L. & Phoenix, G. K. Arctic browning: Impacts of extreme climatic events on heathland ecosystem CO_2 fluxes. *Glob. Change Biol.* **25**, 489–503 (2019).
3. Zhu, Z. et al. Optimality principles explaining divergent responses of alpine vegetation to environmental change. *Glob. Change Biol.* **29**, 126–142 (2023).
4. Gruber, S. Derivation and analysis of a high-resolution estimate of global permafrost zonation. *Cryosphere* **6**, 221–233 (2012).
5. Biskaborn, B. K. et al. Permafrost is warming at a global scale. *Nat. Commun.* **10**, 264 (2019).
6. Smith, S. L., O'Neill, H. B., Isaksen, K., Noetzli, J. & Romanovsky, V. E. The changing thermal state of permafrost. *Nat. Rev. Earth Environ.* **3**, 10–23 (2022).
7. Hu, J., Nan, Z., Ji, H., Zhao, S. & Ou, M. Effect of permafrost degradation on grassland net primary productivity in Qinghai–Tibet Plateau. *Environ. Res. Lett.* **19**, 104051 (2024).
8. Kim, I.-W. et al. Abrupt increase in Arctic-subarctic wildfires caused by future permafrost thaw. *Nat. Commun.* **15**, 7868 (2024).
9. Miner, K. R. et al. Permafrost carbon emissions in a changing Arctic. *Nat. Rev. Earth Environ.* **3**, 55–67 (2022).
10. Kim, J. et al. Carbon response of tundra ecosystems to advancing greenup and snowmelt in Alaska. *Nat. Commun.* **12**, 1–10 (2021).
11. Hoad, C. G., Myers-Smith, I. H., Kerby, J. T., Colesie, C. & Assmann, J. J. Snow persistence lowers and delays peak NDVI, the vegetation

index that underpins Arctic greening analyses. *Environ. Res. Lett.* **20**, 034019 (2025).
12. Li, T. et al. The thickening of the permafrost active layer will negate the promoting effect on vegetation productivity. *Environ. Res. Lett.* **20**, 054042 (2025).
13. Baltzer, J. L. et al. Increasing fire and the decline of fire adapted black spruce in the boreal forest. *Proc. Natl. Acad. Sci.* **118**, e2024872118 (2021).
14. Turetsky, M. R. et al. Carbon release through abrupt permafrost thaw. *Nat. Geosci.* **13**, 138–143 (2020).
15. Devoie, É. et al. Disconnected active layers and unfrozen permafrost: a discussion of permafrost-related terms and definitions. *Sci. Total Environ.* **912**, 169017 (2024).
16. Wang, X. et al. Contrasting characteristics, changes, and linkages of permafrost between the Arctic and the Third Pole. *Earth-Sci. Rev.* **230**, 104042 (2022).
17. Lara, M. J., Nitze, I., Grosse, G., Martin, P. & McGuire, A. D. Reduced Arctic tundra productivity linked with landform and climate change interactions. *Sci. Rep.* **8**, 2345 (2018).
18. Magnússon, R. Í, Groten, F., Bartholomeus, H., van Huissteden, K. & Heijmans, M. M. P. D. Tundra browning in the Indigirka lowlands (North-Eastern Siberia) explained by drought, floods and small-scale vegetation shifts. *J. Geophys. Res.: Biogeosci.* **128**, e2022JG007330 (2023).
19. Phoenix, G. K. & Bjerke, J. W. Arctic browning: extreme events and trends reversing Arctic greening. *Glob. Change Biol.* **22**, 2960–2962 (2016).
20. Pan, N. et al. Increasing global vegetation browning hidden in overall vegetation greening: Insights from time-varying trends. *Remote Sens. Environ.* **214**, 59–72 (2018).
21. Anderegg, W. R. L., Trugman, A. T., Bowling, D. R., Salvucci, G. & Tuttle, S. E. Plant functional traits and climate influence drought intensification and land–atmosphere feedbacks. *Proc. Natl. Acad. Sci.* **116**, 14071–14076 (2019).
22. Li, W. et al. Disentangling effects of vegetation structure and physiology on land–atmosphere coupling. *Glob. Change Biol.* **31**, e70035 (2025).
23. Zona, D. et al. Pan-Arctic soil moisture control on tundra carbon sequestration and plant productivity. *Glob. Change Biol.* **29**, 1267–1281 (2023).
24. Berner, L. T. et al. Summer warming explains widespread but not uniform greening in the Arctic tundra biome. *Nat. Commun.* **11**, 1–12 (2020).
25. Liu, L. et al. Soil moisture dominates dryness stress on ecosystem production globally. *Nat. Commun.* **11**, 1–9 (2020).
26. Beck, P. S. A., Atzberger, C., Høgda, K. A., Johansen, B. & Skidmore, A. K. Improved monitoring of vegetation dynamics at very high latitudes: A new method using MODIS NDVI. *Remote Sens. Environ.* **100**, 321–334 (2006).
27. Wang, S. et al. Temporally corrected long-term satellite solar-induced fluorescence leads to improved estimation of global trends in vegetation photosynthesis during 1995–2018. *ISPRS J. Photogramm. Remote Sens.* **194**, 222–234 (2022).
28. Croft, H. et al. The global distribution of leaf chlorophyll content. *Remote Sens. Environ.* **236**, 111479 (2020).
29. Heijmans, M. M. P. D. et al. Tundra vegetation change and impacts on permafrost. *Nat. Rev. Earth Environ.* **3**, 68–84 (2022).
30. Eyring, V. et al. Overview of the Coupled Model Intercomparison Project Phase 6 (CMIP6) experimental design and organization. *Geosci. Model Dev.* **9**, 1937–1958 (2016).
31. Zhou, S., Zhang, Y., Park Williams, A. & Gentine, P. Projected increases in intensity, frequency, and terrestrial carbon costs of compound drought and aridity events. *Sci. Adv.* **5**, eaau5740 (2019).
32. Sun, J. et al. Why has the inner Tibetan Plateau become wetter since the mid-1990s? *J. Clim.* **33**, 8507–8522 (2020).
33. Chen, T. & Guestrin, C. in Proceedings of the 22nd ACM SIGKDD International Conference on Knowledge Discovery and Data Mining.785–794 (Association for Computing Machinery, 2016 Published).
34. Danesh, T., Ouaret, R., Floquet, P. & Negny, S. in *Computer Aided Chemical Engineering*. 1501–1506 (Elsevier, 2022).
35. Yoshikawa, K. & Hinzman, L. D. Shrinking thermokarst ponds and groundwater dynamics in discontinuous permafrost near Council, Alaska. *Permafr. Periglac. Process.* **14**, 151–160 (2003).
36. Ran, Y. et al. New high-resolution estimates of the permafrost thermal state and hydrothermal conditions over the Northern Hemisphere. *Earth Syst. Sci. Data* **14**, 865–884 (2022).
37. Lara, M. J., Nitze, I., Grosse, G., Martin, P. & McGuire, A. D. Reduced arctic tundra productivity linked with landform and climate change interactions. *Sci. Rep.* **8**, 1–10 (2018).
38. Lund, M. Uncovering the unknown-climate interactions in a changing Arctic tundra. *Environ. Res. Lett.* **13**, 10–1088 (2018).
39. Loranty, M. M. et al. Siberian tundra ecosystem vegetation and carbon stocks four decades after wildfire. *J. Geophys. Res.: Biogeosci.* **119**, 2144–2154 (2014).
40. Hu, F. S. et al. Arctic tundra fires: natural variability and responses to climate change. *Front. Ecol. Environ.* **13**, 369–377 (2015).
41. Swain, D. L. et al. Hydroclimate volatility on a warming Earth. *Nat. Rev. Earth Environ.* **6**, 35–50 (2025).
42. Virkkala, A.-M. et al. Wildfires offset the increasing but spatially heterogeneous Arctic–boreal CO_2 uptake. *Nat. Clim. Change* **15**, 188–195 (2025).
43. Magnússon, R. Í. et al. Rapid vegetation succession and coupled permafrost dynamics in Arctic thaw ponds in the Siberian lowland tundra. *J. Geophys. Res.: Biogeosci.* **125**, e2019JG005618 (2020).
44. Jones, B. M. et al. Lake and drained lake basin systems in lowland permafrost regions. *Nat. Rev. Earth Environ.* **3**, 85–98 (2022).
45. Stocker, B. D. et al. Drought impacts on terrestrial primary production underestimated by satellite monitoring. *Nat. Geosci.* **12**, 264–270 (2019).
46. Li, J., Holmgren, M. & Xu, C. Greening vs browning? Surface water cover mediates how tundra and boreal ecosystems respond to climate warming. *Environ. Res. Lett.* **16**, 104004 (2021).
47. Loiko, S., Klimova, N., Kuzmina, D. & Pokrovsky, O. Lake drainage in permafrost regions produces variable plant communities of high biomass and productivity. *Plants* **9**, 867 (2020).
48. Del Vecchio, J., Palucis, M. C. & Meyer, C. R. Permafrost extent sets drainage density in the Arctic. *Proc. Natl. Acad. Sci.* **121**, e2307072120 (2024).
49. Zou, C., Du, S., Liu, X. & Liu, L. TCSIF: a temporally consistent global Global Ozone Monitoring Experiment-2A (GOME-2A) solar-induced chlorophyll fluorescence dataset with the correction of sensor degradation. *Earth Syst. Sci. Data* **16**, 2789–2809 (2024).
50. Yi, Y. et al. Abrupt thaw and its effects on permafrost carbon emissions in the Tibetan Plateau: A remote sensing and modeling perspective. *Earth-Sci. Rev.* **261**, 105020 (2025).
51. Smith, N. D. et al. Explicitly modelling microtopography in permafrost landscapes in a land surface model (JULES vn5. 4_microtopography). *Geoscientific Model Dev.* **15**, 3603–3639 (2022).
52. Druel, A., Ciais, P., Krinner, G. & Peylin, P. Modeling the vegetation dynamics of northern shrubs and mosses in the ORCHIDEE land surface model. *J. Adv. Modeling Earth Syst.* **11**, 2020–2035 (2019).
53. Druel, A. et al. Towards a more detailed representation of high-latitude vegetation in the global land surface model ORCHIDEE (ORC-HL-VEGv1. 0). *Geoscientific Model Dev.* **10**, 4693–4722 (2017).

54. Miller, P. A. & Smith, B. Modelling tundra vegetation response to recent Arctic warming. *Ambio* **41**, 281–291 (2012).
55. Zhang, W. et al. Tundra shrubification and tree-line advance amplify Arctic climate warming: results from an individual-based dynamic vegetation model. *Environ. Res. Lett.* **8**, 034023 (2013).
56. Meyer, G., Humphreys, E. R., Melton, J. R., Cannon, A. J. & Lafleur, P. M. Simulating shrubs and their energy and carbon dioxide fluxes in Canada's low Arctic with the Canadian Land Surface Scheme Including Biogeochemical Cycles (CLASSIC). *Biogeosciences* **18**, 3263–3283 (2021).
57. Matthes, H. et al. Advances in permafrost representation: biophysical processes in Earth system models and the role of offline models. *Permaf. Periglac. Proc.* **36**, 302–318 (2025).
58. Obu, J., Westermann, S., Kääb, A. & Bartsch, A. Ground Temperature Map, 2000–2016, Northern Hemisphere Permafrost [Data file]. (2018).
59. Loveland, T. R. & Belward, A. S. The IGBP-DIS global 1km land cover data set, DISCover: first results. *Int. J. Remote Sens.* **18**, 3289–3295 (1997).
60. Walker, D. A. et al. The circumpolar Arctic vegetation map. *J. Veg. Sci.* **16**, 267–282 (2005).
61. Beamish, A. et al. Recent trends and remaining challenges for optical remote sensing of Arctic tundra vegetation: A review and outlook. *Remote Sens. Environ.* **246**, 111872 (2020).
62. Savtchenko, A. et al. Terra and Aqua MODIS products available from NASA GES DAAC. *Adv. Space Res.* **34**, 710–714 (2004).
63. Li, M. et al. Spatiotemporally consistent global dataset of the GIMMS Normalized Difference Vegetation Index (PKU GIMMS NDVI) from 1982 to 2022. *Earth Syst. Sci. Data* **15**, 4181–4203 (2023).
64. Dierckx, W. et al. PROBA-V mission for global vegetation monitoring: Standard products and image quality. *Int. J. Remote Sens.* **35**, 2589–2614 (2014).
65. Dierckx, W., Swinnen, E. & Kempeneers, P. Validation of spectral continuity between PROBA-V and SPOT-VEGETATION global daily datasets. *Int. Arch. Photogramm., Remote Sens. Spat. Inf. Sci.* **40**, 1155–1162 (2015).
66. Xu, M. et al. A 21-year time series of global leaf chlorophyll content maps from MODIS imagery. *IEEE Trans. Geosci. Remote Sens.* **60**, 1–13 (2022).
67. Maes, S. L. et al. Environmental drivers of increased ecosystem respiration in a warming tundra. *Nature* **629**, 105–113 (2024).
68. See, C. R. et al. Decadal increases in carbon uptake offset by respiratory losses across northern permafrost ecosystems. *Nat. Clim. Change* **14**, 853–862 (2024).
69. Rodell, M. et al. The global land data assimilation system. *Bull. Am. Meteorological Soc.* **85**, 381–394 (2004).
70. Hersbach, H. et al. ERA5 hourly data on single levels from 1979 to present. https://doi.org/10.24381/cds.adbb2d47. (2018).
71. Castellvi, F., Perez, P. J., Villar, J. M. & Rosell, J. I. Analysis of methods for estimating vapor pressure deficits and relative humidity. *Agric. For. Meteorol.* **82**, 29–45 (1996).
72. Howell, T. A. & Dusek, D. A. Comparison of vapor-pressure-deficit calculation methods—southern high plains. *J. Irrig. Drain. Eng.* **121**, 191–198 (1995).
73. Westermann, S. et al. ESA Permafrost Climate Change Initiative (Permafrost_cci): Permafrost active layer thickness for the Northern Hemisphere, v5.0. NERC EDS Centre for Environmental Data Analysis, 2025. https://doi.org/10.5285/A6FBEDD8EE5B472C8E84E55F746C1704. https://catalogue.ceda.ac.uk/uuid/ecc8890023754cd8853d5e3f7e08b0b0
74. Dobiński, W. Permafrost active layer. *Earth-Sci. Rev.* **208**, 103301 (2020).
75. Poggio, L. et al. SoilGrids 2.0: Producing soil information for the globe with quantified spatial uncertainty. *SOIL* **7**, 24 (2021).
76. Eklundh, L. & Jönsson, P. TIMESAT 3.3 with seasonal trend decomposition and parallel processing Software Manual. (Lund and Malmo University, Sweden, 2017).
77. Tan, B. et al. An enhanced TIMESAT algorithm for estimating vegetation phenology metrics from MODIS data. *IEEE J. Sel. Top. Appl. Earth Observ. Remote Sens.* **4**, 361–371 (2010).
78. Chuvieco, E. et al. MODIS Fire_cci burned area pixel product, version 5.1. Centre for Environmental Data Analysis (2018).
79. Carroll, M. L. et al. MOD44W: Global MODIS water maps user guide. *Int. J. Digit. Earth* **10**, 207–218 (2017).
80. Brenning, A. Interpreting machine-learning models in transformed feature space with an application to remote-sensing classification. *Mach. Learn.* **112**, 3455–3471 (2023).
81. Hussain, M. M. & Mahmud, I. pyMannKendall: a Python package for non parametric Mann Kendall family of trend tests. *J. Open Source Softw.* **4**, 1556 (2019).
82. Nachar, N. The Mann - Whitney U: a test for assessing whether two independent samples come from the same distribution. *Tutor. Quant. Methods Psychol.* **4**, 13–20 (2008).
83. Jordahl, K. et al. (2020, July 15). geopandas/geopandas: v0.8.1 (Version v0.8.1). Zenodo. https://doi.org/10.5281/zenodo.3946761

Acknowledgements

We thank Dr. Zhanzhang Cai from Lund University for providing the MODIS phenology data extracted from TIMESAT, and Prof. Feng Tian for providing the processed SPOT-VGT data, as well as Dr. Mingzhu Xu for generating the FCC data.

Author contributions

Conceptualization: M.W., Y.R., O.S.; Writing – Original Draft: M.W., O.S.; Data Curation: S.W., W.Z., Y.R.; Formal analysis: M.J.L., P.C., H.W.C., B.E., A.C., X.L., Y.Y., C.P., D.C.; Writing – Review & Editing: all authors contributed review and editing of this manuscript.

Funding

This study is jointly supported by the National Key Research and Development Program of China (2024YFF0810900, M.W.), the National Natural Science Foundation of China (42525105, Y.R.; 42111530184, M.W.), the Fundamental Research Funds for the Central Universities (2026300415, M.W.) and the International Science and Technology Cooperation Program under the 2023 Shanghai Action Plan for Science, Technology and Innovation (23230712800, Y.Y.). O.S. acknowledges funding through the Canada Research Chair (award CRC-2018-00259) and NSERC Discovery Grants programs (award DGPIN-2018-05743). B.E. is supported from the Danish National Research Foundation (CENPERM DNRF100). M.J.L. is supported by NASA-ABoVE (80NSSC22K1254), NSF-EnvE (1928048), and DOE-TES (DE-SC0021094). H.W.C. is supported by ModElling the Regional and Global Earth system (MERGE) and STINT (CH2020-8799). W.Z. is supported by grants from the Swedish Research Council (VR 2020-0533) and the Swedish Strategic Research Areas Biodiversity and Ecosystem Services in a Changing Climate (BECC) and MERGE. C.P. is supported by the Joint Fund for Regional Innovation and Development of the National Science Foundation (U22A20570). D.C. is supported by Carbon Neutrality and Energy System Transformation (CNEST) Program and Tsinghua University (100008001).

Competing interests

The authors declare no competing interests.

Additional information

Supplementary information The online version contains supplementary material available at https://doi.org/10.1038/s41467-026-75131-4.

Correspondence and requests for materials should be addressed to Mousong Wu, Oliver Sonnentag or Youhua Ran.

Peer review information *Nature Communications* thanks José Grünzweig and the other, anonymous, reviewer(s) for their contribution to the peer review of this work. A peer review file is available.

[1]International Institute for Earth System Science, Nanjing University, Nanjing, China. [2]Département de géographie, Université de Montréal, Montréal, QC, Canada. [3]Department of Plant Biology, University of Illinois, Urbana, IL, USA. [4]Department of Geography, University of Illinois, Urbana, IL, USA. [5]National Cryosphere Desert Data Center, State Key Laboratory of Cryospheric Science and Frozen Soil Engineering, Northwest Institute of Eco-Environment and Resources, Chinese Academy of Sciences, Lanzhou, China. [6]Department of Environmental and Energy Sciences, Chalmers University of Technology, Gothenburg, Sweden. [7]School of Geographical and Earth Sciences, University of Glasgow, Glasgow, UK. [8]Department of Earth and Environmental Sciences, Lund University, Lund, Sweden. [9]Laboratoire des Sciences du Climat et de l'Environnement, IPSL, CEA-CNRS-UVSQ, Université Paris-Saclay, Gif Sur Yvette, France. [10]Center for Permafrost (CENPERM), Department of Geosciences and Natural Resource Management, University of Copenhagen, Copenhagen, Denmark. [11]National Tibetan Plateau Data Center (TPDC), State Key Laboratory of Tibetan Plateau Earth System, Environment and Resources (TPESER), Institute of Tibetan Plateau Research, Chinese Academy of Sciences, Beijing, China. [12]Department of Biology and Graduate Degree Program in Ecology, Colorado State University, Fort Collins, CO, USA. [13]College of Agriculture, Nanjing Agricultural University, Nanjing, China. [14]College of Surveying and Geo-informatics, Tongji University, Shanghai, China. [15]Department of Biology Sciences, University of Quebec at Montreal, Montreal, QC, Canada. [16]School of Geographic Sciences, Hunan Normal University, Changsha, China. [17]Department of Earth System Science, Tsinghua University, Beijing, China. [18]Institute for Carbon Neutrality, Tsinghua University, Beijing, China. ✉e-mail: mousongwu@nju.edu.cn; oliver.sonnentag@umontreal.ca; ranyh@lzb.ac.cn